Journal of Instrumentation

PAPER • OPEN ACCESS

Secondary scintillation properties of multi-layer THGEMs operated in low-pressure CF_4 and Ar/5%Xe

To cite this article: M. Cortesi *et al* 2023 *JINST* **18** P08005

Jinst

Published by IOP Publishing for Sissa Medialab

Received: *January 17, 2023*
Revised: *April 6, 2023*
Accepted: *July 10, 2023*
Published: *August 4, 2023*

Secondary scintillation properties of multi-layer THGEMs operated in low-pressure CF_4 and Ar/5%Xe

M. Cortesi,[a,*] **H. Sims,**[a] **J. Pereira,**[a] **Y. Ayyad,**[b] **P.A. Majewski**[c] **and I. Katsioulas**[d]

[a] *Facility for Rare Isotope Beams, Michigan State University, East Lansing, MI 48824, U.S.A.*
[b] *IGFAE, Universidade de Santiago de Compostela, E-15782 Santiago de Compostela, Spain*
[c] *Particle Physics Department, STFC Rutherford Appleton Laboratory, Didcot, OX11 0QX, U.K.*
[d] *Instruments Division, European Spallation Source ESS ERIC (ESS), Box 176, SE-221 00 Lund, Sweden*

E-mail: cortesi@frib.msu.edu

Abstract: We present a measurement of the secondary scintillation yield produced by two-layer Thick Gas Electron Multipliers (M-THGEMs) in pure Tetrafluoromethane (CF_4) gas and in Ar mixed with 5% Xe in low-pressures down to 20 Torr. The detector was irradiated with 5.49 MeV alpha particles from a low-rate 241-Am source. The secondary scintillation light generated during the gas avalanche process was read out by a Hamamatsu photomultiplier tube (model R8520-406), sensitive to a broad wavelength range (160–650 nm). The avalanche charge was collected on the bottom electrode of M-THGEM and correlated to the scintillation light on an event-by-event basis. We observed that, for both gas types, the value of the photon to electron production ratio (0.4 ph/el in CF_4 and 0.1 ph/el in Ar/5%Xe) increases with the thickness of the M-THGEM electrodes and varies significantly with the pressure, being higher at lower values. The decrease in electroluminescence yield at higher pressures is much more pronounced in the Ar/Xe mixture. In addition, because of a larger gas avalanche volume, the electroluminescence light yield is larger in thicker M-THGEM structures. Presented results are particularly useful for designing the next generation of Optical-readout Time Projection Chambers (O-TPCs) operated at low-pressure CF_4; applications include experimental nuclear physics with rare isotope beams, dark matter detection with directional sensitivity and observation of the Migdal effect in a low-pressure Optical TPC.

Keywords: Dark Matter detectors (WIMPs, axions, etc.); Optical detector readout concepts; Time projection chambers

*Corresponding author.

https://doi.org/10.1088/1748-0221/18/08/P08005

2023 JINST 18 P08005

Contents

1 **Introduction** 1

2 **Material and method** 2

3 **Results** 6

4 **Summary and conclusion** 9

2023 JINST 18 P08005

1 Introduction

In the last few years, significant progress has been made in the field of particle detection using gaseous scintillation counting [1]. Recent advances in the field are mainly due to the implementation of novel sensitive photon detection technologies characterized by enhanced sensitivity, low noise, wide dynamic range extended from the visible to extreme ultraviolet (EUV) range, fast frame-rate capability and excellent granularity [2–4]. High energy resolution and excellent tracking capability are the outstanding merits of the newly developed gaseous scintillation counting technique.

Micro-pattern gas detector structures, installed in a high scintillation-yield gas volume, have been shown to generate a number of photons during the avalanche process [5–8]. Those photons are the result of inelastic collisions between avalanche electrons and gas molecules and they can be detected, for instance, with a charged-coupled device (CCD) camera for localization capability. Modern gas avalanche detectors with optical readout (vacuum photomultipliers and CCD cameras) are typically used in time projection chambers (TPCs) for rare event detection experiments, such as direct dark matter searches and double beta decay experiments [1].

This work systematically investigates the secondary scintillation light emission properties of Tetrafluoromethane (CF_4) and Ar/5%Xe generated by novel two-layer M-THGEM structures [9]. The latter is characterized by a thick gas avalanche volume, several times larger than the electron mean-free path at low pressure, which provides stable high-gain operation. High scintillation yield is needed to guarantee optimal performance of optical readout, both in terms of energy resolution and tracking capability.

The nature of the scintillating gas fillings exploited in this work is chosen based on two main characteristics: a high maximum achievable gain at low pressure and a large scintillation yield. CF_4 was considered as a filling gas medium because of its large visible light emission, which is easily detectable with commercially available photon sensors. Ar and Xe are both excellent light emitters. Small amounts of Xe would serve to shift the scintillation light of Ar to the characteristic emission of Xe, which can be detected with CsI-based photocathodes.

A key objective of the present work is to develop optical readout TPCs that can be applied to nuclear physics, including the study of nuclear reactions with rare isotope beams [10, 11] and the measurement of cross sections crucial to stellar evolution theory [12]. Due to their compelling

capabilities, the use of conventional TPCs with charge readout for low-energy nuclear studies has grown to a remarkable extent over the last few years [10]. Implantation-decay experiments benefit from the TPC´s low detection threshold and large detection efficiency for the measurement of charged particles emitted in the decay of a radioactive isotope implanted inside the sensitive volume. If the energy of the particle to detect is small, such as those emitted from resonances near the emission threshold or heavy residues from a scattering interaction, TPCs are the reliable path to high-quality measurements. Because of the larger granularity of optical sensors, such as CCD cameras with respect to conventional charge readouts for TPCs, the use of scintillating low-pressure gas as a tracking medium will lower the limits of detection when measuring low-energy heavy ions. Optical TPCs may provide better angular resolution, lower detection threshold, and improved particle identification capabilities. Rare nuclear decays [11] and reactions of astrophysical interest [12] are particularly well suited to leverage low-pressure scintillating gases for the operation of M-THGEM detectors.

Finally, the implementation of the novel optical readout M-THGEM based structure may be of particular interest in rare event searches where the detection mechanism is based on direct imaging of keV-MeV recoil tracks. A higher sensitivity to a small-energy tracking capability may open the way towards applications such as directional dark matter [13, 14], sub-GeV solar neutrinos [15], solar axions [16], and Migdal effect measurements [17]. In particular, the Migdal approach would significantly impact several experiments which expect to extend their limits to lighter DM masses [18].

2 Material and method

The experimental setup used in this work to measure the properties of electron avalanche processes and avalanche-induced photon emission is schematically illustrated in figure 1. All the detector system components were installed in a light-tight, large-volume stainless-steel vessel, equipped with a dedicated gas handling system. The latter supplies the gas filling (CF_4 or Ar/5%Xe) to the detector vessel at a pressure ranging from 100 to 20 Torr, with a regulated gas flow typically of 25–30 sccm. Before any gas introduction, the vessel was evacuated down to a few μTorr with a turbo-molecular pump.

The M-THGEM was mounted on FR4 mechanical support using thin Teflon rods. The FR4 support had a circular, 7 cm in diameter aperture that allowed the avalanche light to be recorded by a photomultiplier tube (Hamamatsu PMT model R8520-406) facing the bottom electrode of the M-THGEM. A thin metal mesh was mounted 1.5 cm from the M-THGEM top surface, defining the drift region. A constant reduced electric field of 12 Volt/cm/Torr was applied in the drift region by a suitable voltage difference between the top M-THGEM surface and the mesh. The same reduced electric field applied to the drift region was used for all the measurements presented in this work. The bias voltage for all three M-THGEM electrodes and the PMT was supplied by a digital-controlled high-voltage power supply (ISEG model EHS). The PMT's voltage-divider circuit was designed according to Hamamatsu specifications.

Two different two-layer M-THGEM structures have been investigated: (1) made of FR4, (figure 2(a)) and characterized by a total thickness of 1.6 mm, 0.8 mm hole pitch, 0.4 mm hole diameter, and 0.1 mm hole rim; (2) made of ceramic (figure 2(b)) with a total thickness of 1.1 mm, 0.8 mm hole pitch, 0.25 mm hole diameter, and 0.1 mm hole rim.

2023 JINST 18 P08005

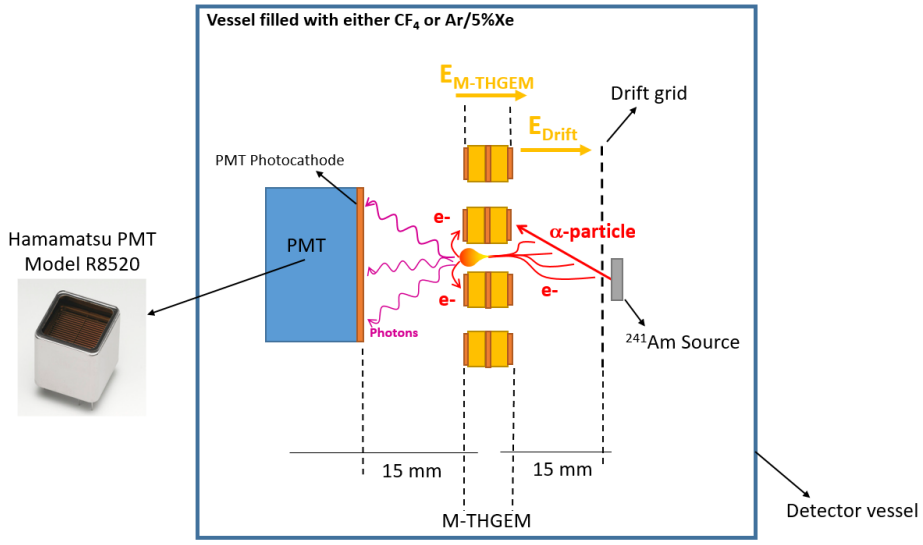

Figure 1. Schematic drawing of the experimental setup (not to scale).

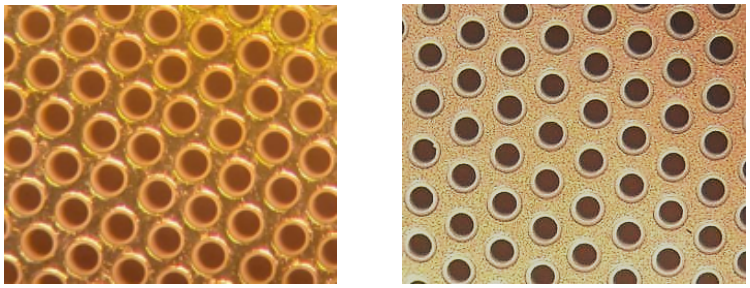

(a) (b)

Figure 2. Details of the FR4 M-THGEM (part a) and the ceramic one (part b).

The detector was irradiated by 5.49 MeV alpha particles emitted by a weak 241-Am source, placed on top of the drift mesh. The alpha particles, emitted with a rate of about 500 Hz, crossing the drift region release a number of ionization electrons (primaries) and an amount of primary scintillation light proportional to the amount of energy lost in the gas. The ionization electrons drift towards and are funnelled into M-THGEM holes, where they are subjected to gas avalanche multiplication under the influence of a high electric field. This generates more scintillation light (secondary scintillation). Because of the small amount of energy released in the low-pressure gas, and because of the low optical transparency of the M-THGEMs (being about 45% for the FR4 structure and about 18% for the ceramic one), the primary scintillation light detected by the PMT is negligible compared to the secondary light produced during the avalanche process. While optical transparency does not affect the performance of detection of light from gas avalanche multiplication, and although it is not relevant to the measurements presented in this article, it should be noted that PMTs can be placed on the drift grid side for future studies if detection of primary scintillation is critical.

The gas-avalanche electrons generated in the M-THGEM holes were collected on the M-THGEM bottom electrode and then processed by a charge-sensitive preamplifier (Tennelec, Model 178) —

2023 JINST 18 P08005

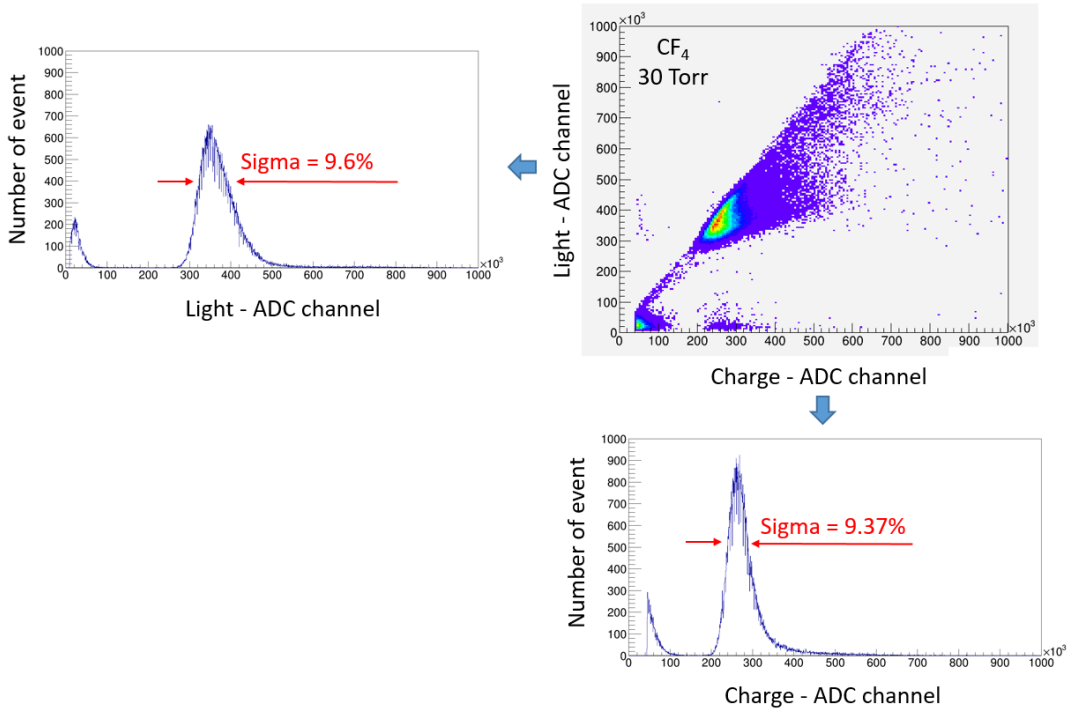

Figure 3. Example of a light-charge correlation map recorded in CF_4 at 30 Torr. The projections of the light-charge correlation map, corresponding to the light and charge ADC spectra, are also shown.

charge output. The same type of preamplifier was used to process the output of the PMT — light output. The charge and light outputs were further processed and digitized using the FASTER-ADC modular acquisition system [19]. The latter provides a digital shaper discriminator-peak and hold function for simultaneous energy spectra measurements.

Figure 3 shows an example of the light-charge map density generated by recording around 120,000 events. For the data shown in the figure, the detector was filled with CF_4 at 30 Torr and a voltage difference of 500 V was applied to each of the two multiplication stages of the 1.6 mm thick M-THGEM. The high density of events displayed along a narrow linear distribution in the map underlines the significant correlation between avalanche light and charge. Due to poor collimation of the 241-Am source placed above the drift region, a considerable fraction of alpha particles crossed the drift area at wide angles, releasing a higher number of primary ionization electrons. In such large-angle events, the avalanche light produced in the M-THGEM holes is partially screened by the M-THGEM substrate, resulting in a loss of light-charge proportionality. As a result, the 5.49 MeV alpha particle peak appears to extend over a large area of the low scintillation yield area. Moreover, the peak in the light spectrum appears slightly asymmetric; however, this effect is negligible and did not affect the scintillation yield calculation.

The figure also shows the projected X and Y coordinates, corresponding to the charge and light spectrum, respectively. In the light and charge spectra, the 5.49 MeV alpha particle peaks have very similar features; both are characterized by a width (RMS) of 9.37% and 9.6%, respectively.

The calibration of the ADC channels (henceforth denoted as Cal_{charge} for the charge signals, and Cal_{light} for the light output) was accomplished using a 10 pF test input on the preamplifier [20]. By

2023 JINST 18 P08005

injecting known voltages across the input capacitor, well-defined charge signals propagate through the electronic chain. The calibration fit was obtained using several charge signals covering the entire amplitude range of the analysed charge (M-THGEM) and light (PMT) spectra. The number of primary ionization electrons released by the 5.49 MeV alpha particles in the 15 mm drift gap was computed for different pressures and different gas fillings (CF_4 and Ar/Xe mixture) using the SRIM software package [21]. The average energy to produce an electron-ion pair, W, for α particles (initial energy $\sim$ 5.49 MeV) is 34.3 eV and 26.3 eV per ion pair in CF_4 and Ar/5%Xe, respectively [22]. Once the calibration factors were established, the charge avalanche gain provided by the M-THGEM was simply calculated as the product of the charge calibration factor and the centroid of the 5.49 MeV peak, divided by the calculated number of primaries.

$$\text{GAIN} = \frac{\text{Avalanche electrons}}{\text{Primaries}} = \frac{\text{ADC}_{\text{charge}} \cdot \text{Cal}_{\text{charge}}}{\text{Primaries}} \tag{2.1}$$

Finally, the light yield (number of avalanche photons/number of avalanche electrons) was calculated using the following equation:

$$\text{Y} = \frac{\text{Avalanche Photons}}{\text{Avalanche Electrons}} = \frac{\text{ADC}_{\text{light}} \cdot \text{Cal}_{\text{light}}}{\text{ADC}_{\text{charge}} \cdot \text{Cal}_{\text{charge}}} \cdot \frac{4\pi}{\Omega} \cdot \frac{1}{\text{GAIN}_{\text{PMT}} \cdot \text{PDE}} \tag{2.2}$$

where

- $\text{ADC}_{\text{light}}$ and $\text{ADC}_{\text{charge}}$ are the centroids of the alpha particle peaks in the recorded light and charge spectra, respectively.
- Ω is a measure of the effective solid angle seen by the PMT. It was computed with a Monte Carlo method taking into account different factors, including the size of the detector area irradiated by the 241-Am source, the PMT photocathode area, and the distance between the PMT photocathode and the M-THGEM electrode.
- the GAIN_{PMT} factor is the current gain of the PMT, which depends on the operational voltage applied to the voltage-divider circuit. Based on the operational conditions, GAIN_{PMT} was extracted from the Hamamatsu R8520 datasheet [23]. The voltage-divider circuit used to bias the PMT was designed according to Hamamatsu specifications.
- PDE (photo-detection efficiency) is the anode sensitivity of the PMT and it was estimated by convoluting the spectral response of the PMT (i.e., the photon detection efficiency as a function of the photon wavelength — see Hamamatsu R8520 datasheet [23]) with the characteristic scintillation emission spectrum of the filling gas [24, 25]. For the Ar/Xe mixture, we have assumed that the light detected by the PMT was shifted to the characteristic xenon emission, at 178 nm, for which the PMT has a PDE of 30%. Considering both UV and visible emission components of CF_4, the PMT PDE is estimated to be 14%.

Based on equation (2.2), the charge and light produced during the avalanche processes are measured and used as inputs for the calculation to obtain the scintillation yield. The uncertainty in the calculated scintillation yield (Y) is attributed several factors, including the error in the calibration of the ADC spectrum used with light and charge electronics, the error in the assumed value of the

2023 JINST 18 P08005

photon-detection efficiency, and the error in the calculation of the solid angle detected by the PMT. According to our estimation, the uncertainty in calculating Y is mainly due to errors in estimating the solid angle Ω. As a matter of fact, the PMT sees a different solid angle depending on where the avalanche occurs. The solid angle's value is maximum when the avalanche occurs directly in front of the PMT, and it diminishes when it is farther away. Our method of estimating the average solid angle has been based on a Monte Carlo simulation: we generated a number of avalanches at different locations on the M-THGEM surface using a uniform random number generator and calculated the solid angle seen from the effective area of the PMT photocathode. We used a fixed value for the distance between the PMT and the M-THGEM, and the nominal sensitive area of the PMT provided by the Hamamatsu datasheet. However, this method does consider some minor effects like the screening of the light by the M-THGEM hole when the avalanche is not centred with respect to the PMT location, and the long track of the particle in the drift region, which causes multiple avalanche points on the M-THGEM surface. As a result, we have estimated the uncertainty on Y derived from the estimated solid angle to be around 25–30%. The errors in the ADC calibration and the one derived from the estimated PDE are definitely smaller (several percent).

3 Results

Figure 4 illustrates the measured gas gains as a function of the reduced voltage difference (Volt/Torr) symmetrically applied to each of the two multiplication stages of the 1.6 mm thick M-THGEM, measured in CF_4 (part a) and Ar/5%Xe (part b), at different pressures. In all measurements, the maximum achievable gain was defined by the onset of discharges within the M-THGEM holes, which are triggered when the Raether limit is reached — namely when the maximum amount of charge accumulated in an avalanche (the sum of primary and secondary electrons) approaches the 10^{-7}–10^{-8} electron-ion pair regime [26]. The decrease in maximum achievable gain as the pressure increases, as shown in figure 4, is caused by the larger number of primaries produced by alpha particles in the drift region; a large number of primaries triggers a transition from a stable proportional mode to discharges at lower gains. However, the total number of electrons at the highest achievable gain approaches the value of 10^7 electrons for all investigated pressures. Note that the amount of electroluminescence light is proportional to the total number of electrons occurring in the gas avalanche process.

Figure 5 part (a) illustrates an example of comparison between the total number of avalanche electrons and the total number of avalanche scintillation photons recorded in CF_4 (part a) and Ar/5%Xe (part b) at 20 Torr as a function of the voltage difference between the FR4 M-THGEM electrodes. Each data point in the graph was extracted from the analysis of charge and light spectra (see figure 3) recorded by the FASTER-ADC. The value of each data point was computed by converting the centroid of the alpha particle peaks into a number of electrons or photons, using the appropriate calibration factor. The scintillation yield for every data set is thus computed as the light-to-charge ratio. As shown in figure 5 part (c), the scintillation yield measured at 20 Torr approached a constant value of 0.4 photon/electron in CF_4 and slightly above 0.1 photon/electron in Ar/5%Xe. The charge-light correlations were quite strong for both gas mixtures, resulting in a constant scintillation yield over the extensive range of voltage bias applied to the M-THGEM. That means the scintillation yield does not depend on the avalanche size.

2023 JINST 18 P08005

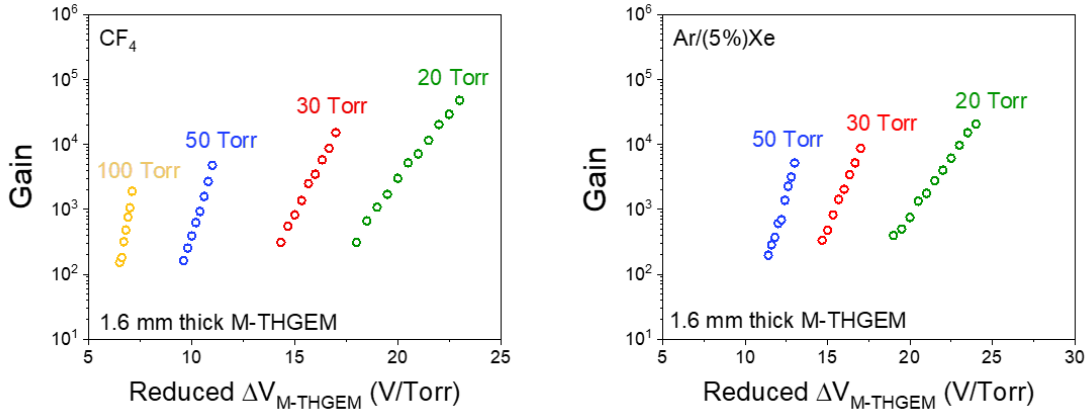

(a) (b)

Figure 4. Absolute gain of a 1.6 mm M-THGEM measured in CF_4 (part a) and in Ar/5%Xe (part b) at low pressure. The detector was irradiated by 5.49 MeV alpha particles from a 241-Am source.

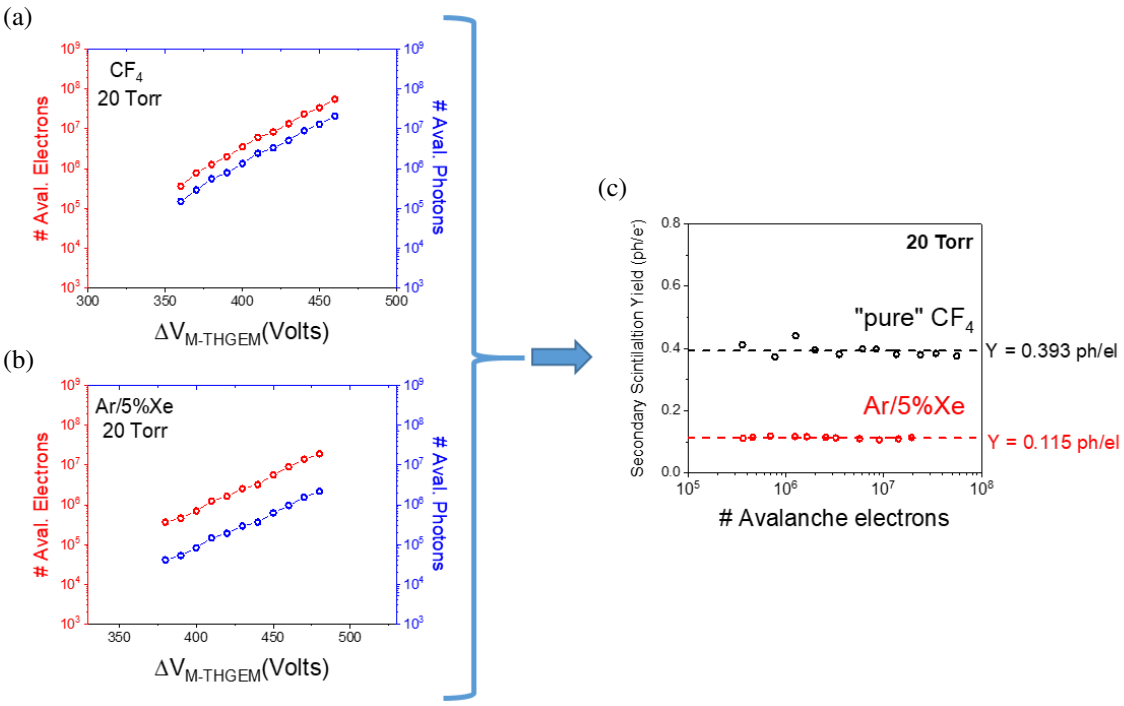

Figure 5. Part (a) and (b) show an example (20 Torr CF_4) of comparison between avalanche charge (number of electrons, in red graph) and avalanche light (number of photons, in the blue graph) as a function of the voltage difference applied across each FR4 M-THGEM (1.6 mm thick) multiplication stage. Measurements were performed in CF_4 (part a) and in Ar/5%Xe (part b) at 20 Torr. Part (c) shows the calculated secondary scintillation yield Y (photon/electron) as a function of the total number of avalanche charge computed for data depicted in part (a) and (b).

2023 JINST 18 P08005

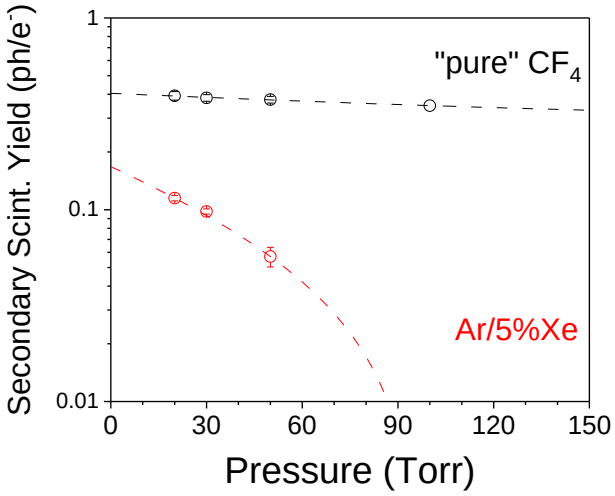

Figure 6. Scintillation yield measured in CF_4 (black graph) and in Ar/5%Xe as a function of the pressure.

Similar measurements and analyses were done at 20, 30, 50 and 100 Torr in CF_4 (figure 6, black graph), and at 30 and 50 Torr in Ar/5%Xe (figure 6, red graph). The same charge/light trends shown in figure 5, resulting in a constant scintillation light yield, were obtained in all the investigated pressures and over a wide charge gains (up to the maximum achievable gain), for both scintillating gases. As shown in figure 6, there is a systematic decrease in the scintillation yield as gas pressure increases for both gas mixtures. However, while in CF_4 the loss of scintillation yield is around 13% when the pressure rises from 20 to 100 Torr, in Ar/5%Xe the decrease is more pronounced, corresponding to about 50% when the pressure increases from 20 to 50 Torr.

Finally, figure 7 compares the secondary scintillation yield measured in CF_4 using two different M-THGEM electrodes: a 1.6 mm thick FR4 electrode (blue graph) and a 1.1 mm thick ceramic one (red graph). The longer avalanche volume of the thicker M-THGEM electrode enables larger production of secondary scintillation light.

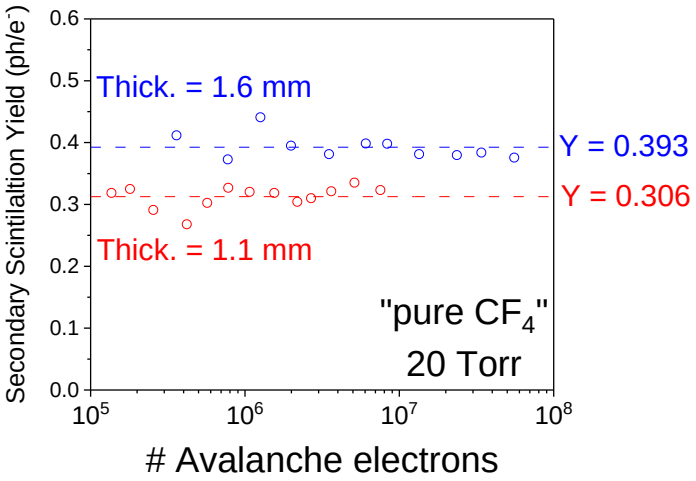

Figure 7. Scintillation yield measured in CF_4 at 20 Torr, produced in 1.6 mm thick FR4 M-THGEM (blue graph) and in 1.1 mm ceramic one (red graph).

2023 JINST 18 P08005

This is very similar to the case of the proportional scintillation mode, in which the light yield (defined as the number of secondary scintillation photons produced per drifting electron per unit path length) is proportional to the gas gap in which the electroluminescence is emitted [27]. In this case, light emission occurs when electrons produced during primary ionization are accelerated by the applied field and collide with noble gas atoms or with impurity molecules without further ionization, namely without charge multiplication.

4 Summary and conclusion

This work presents and discusses the results of systematic measurements of secondary scintillation yield produced in M-THGEM structures. The latter was operated in CF_4 and Ar/5%Xe at low pressure (20–100 Torr), and was irradiated by 5.49 MeV alpha particles (241-Am source).

The correlation between light and charge signals that originated during the gas avalanche, on an event-by-event basis, was investigated using a two-channel ADC. The M-THGEM achieved total ionization of about 10^7 before the onset of a discharge, in all assessed conditions (gas type, pressure, M-THGEM geometry). The highest number of scintillation photons per avalanche electron was attained with the thicker (1.6 mm) M-THGEM at the lower gas pressure (20 Torr) for both gas mixtures, being around 0.4 photon/electron in CF_4 and 0.1 photon/electron in Ar/5%Xe. It was observed that if the avalanche volume is larger (i.e., a thicker M-THGEM substrate), then the production of secondary scintillation light is proportionally higher.

The M-THGEM architecture provides stable high-gain operation at low pressure and for different gas mixtures. CF_4 has generated a better secondary scintillation light yield than Ar/5%Xe. Further investigation with a combination of Ar mixed with other secondary gases as a wavelength shifter will be considered in future studies, including CF_4 and CH_4. It was observed that for both gas mixtures, the scintillation yield decreases as the gas density increases. The variation of light yield with density in Ar/5%Xe is significantly greater than the one measured in CF_4.

Note that the processes and the nature of secondary scintillation light in CF_4 are very different from those that characterize Ar/Xe emission. Though the origin of the scintillation process in CF_4 and the nature of the possible emitting states are not fully understood [28–30], it is believed that light is mostly generated by the various excited states of the atomic fluorine F^* and of the CF_3^{+*} radical. These two species, in turn originate from two-fragment dissociation via the following process [30]:

$$e + CF_4 \rightarrow CF_4^{**} \rightarrow CF_3^{+*} + F^* \tag{4.1}$$

The formation of radiating metastable fragments described above competes with other non-radiative single-electron impact mechanisms. The decay pathway, characteristic relaxation times, and the relative cross-section lead to the progress of the various excited electronic states of CF_4 molecules [28]. These also include a rearrangement of the energy distribution of the excited states by molecular collisions — this latter factor depends on the gas density, and we may speculate that this is the major cause of the small drop in the scintillation yield in CF_4 at higher gas number densities (i.e. gas pressure).

In Ar/Xe mixtures, the characteristic emission of the heavier Xe component (at 178 nm) dominates the Ar continuum (at 127 nm), even when it is present only in traces — see figure 9 in ref. [1] and also [31, 32]. The spectra of a mixture containing just a few percent Xe are similar to the spectra of pure Xe. In this case, the light emission is a two-step process: electron-induced

2023 JINST 18 P08005

Ar ionization/excitation, followed by atomic collisions that lead to the energy transfer from the Ar to the Xe atom, and the formation of the Xe excited states. The excitation transfer can occur from the Ar_2^* dimers or atomic precursor states (Ar*, Ar^+). The final emission originates from the sequential formation of excited dimers Xe_2^* favored through three-body collisions. Those emissions are centred at 147 nm (first continuum) and 172 nm (second continuum). The first and second continuum correspond to the VUV radiative decay of the vibrational $(Xe_2^*)^{\upsilon}$ excited and $(Xe_2^*)^{\upsilon=0}$ relaxed excimer states, respectively [32–34]. However, only above 300 Torr the second continuum is dominant, and the secondary scintillation presents only a narrow peak centred at 172 nm. In the pressure range investigated in this work (20–100 Torr), a significant component is still emitted in the first continuum, for which our optical detector system (the Hamamatsu PMT) is blind.

Similarly to the CF_4 case, in the Ar/Xe mixture the efficiency of the transfer process depends on several factors: the lifetime of the excitation states of the Ar and Ar_2^* dimers (single, triplet); the presence of resonance states in which the energy coincides with that of the emission of the donor gas; the partial pressure of the Xe, and the density of the gas (pressure) that affect the mean free paths, and thus the frequency of the atomic/molecular collisions. As the pressure increases, more non-radiative transitions will occur, diminishing the net energy available for scintillation light. Impurities may also be responsible for quenching the characteristic Xe emission. All these phenomena contribute to the significant drop in scintillation light as pressure rises.

The M-THGEM geometries investigated in this work have been proven to achieve stable high gains in low-pressure (up to 100 Torr) scintillating gas mixtures (specifically CF_4 and Ar/5%Xe). As a result of the large avalanche charge gain and the large avalanche volume in the M-THGEM, it has been demonstrated that it is possible to produce high scintillation light for low-energy detection limits and accurate tracking capabilities. This opens the way to the implementation of M-THGEM based optical readout for low-pressure TPCs applied to nuclear physics with rare isotope beams, dark matter detection with directional sensitivity and the observation of the Migdal effect.

Acknowledgments

This material is based upon work supported by the U.S. Department of Energy Office of Science under Cooperative Agreement DE-SC0000661, the State of Michigan and Michigan State University. H. Sims was supported by the NSF Division of Physics award no. PHY-2050733, "Research Experiences for Undergraduates at Michigan State University". The authors acknowledge the support of the RD51 collaboration in providing the M-THGEM elements tested in this work.

References

[1] D. Gonzalez-Diaz, F. Monrabal and S. Murphy, *Gaseous and dual-phase time projection chambers for imaging rare processes*, *Nucl. Instrum. Meth. A* **878** (2018) 200 [arXiv:1710.01018].

[2] J.-F. Pratte et al., *3D Photon-To-Digital Converter for Radiation Instrumentation: Motivation and Future Works*, *Sensors* **21** (2021) 598.

[3] L. Sang, M. Liao and M. Sumiya, *A Comprehensive Review of Semiconductor Ultraviolet Photodetectors: From Thin Film to One-Dimensional Nanostructures*, *Sensors* **13** (2013) 10482.

2023 JINST 18 P08005

[4] R. Galea et al., *Light yield measurements of GEM avalanches at cryogenic temperatures and high densities in neon based gas mixtures.*, *IEEE Nucl. Sci. Symp. Med. Imaging Conf.* **1** (2007) 239.

[5] A. Badertscher et al., *First operation of a double phase LAr Large Electron Multiplier Time Projection Chamber with a two-dimensional projective readout anode*, *Nucl. Instrum. Meth. A* **641** (2011) 48 [arXiv:1012.0483].

[6] A. Cools et al., *Neutron and beta imaging with Micromegas detectors with optical readout*, *Nucl. Instrum. Meth. A* **1048** (2023) 167910.

[7] C. Li et al., *An optical fiber-based flexible readout system for micro-pattern gas detectors*, 2018 *JINST* **13** P04013.

[8] M. Marafini et al., *ORANGE: A high sensitivity particle tracker based on optically read out GEM*, *Nucl. Instrum. Meth. A* **845** (2017) 285.

[9] M. Cortesi et al., *Multi-layer thick gas electron multiplier (M-THGEM): A new MPGD structure for high-gain operation at low-pressure*, *Rev. Sci. Instrum.* **88** (2017) 013303 [arXiv:1606.07314].

[10] D. Bazin et al., *Low energy nuclear physics with active targets and time projection chambers*, *Prog. Part. Nucl. Phys.* **114** (2020) 103790.

[11] Y. Ayyad et al., *Direct observation of proton emission in ^{11}Be*, *Phys. Rev. Lett.* **123** (2019) 082501 [*Erratum ibid.* **124** (2020) 129902] [arXiv:1907.00114].

[12] T. Budner et al., *Constraining the $^{30}P(p,\gamma)^{31}S$ Reaction Rate in ONe Novae via the Weak, Low-Energy, β-Delayed Proton Decay of ^{31}Cl*, *Phys. Rev. Lett.* **128** (2022) 182701 [arXiv:2204.05444].

[13] F. Mayet et al., *A review of the discovery reach of directional Dark Matter detection*, *Phys. Rept.* **627** (2016) 1 [arXiv:1602.03781].

[14] S.E. Vahsen et al., *CYGNUS: Feasibility of a nuclear recoil observatory with directional sensitivity to dark matter and neutrinos*, arXiv:2008.12587.

[15] F. Arzarello et al., *HELLAZ: a high rate solar neutrino detector with neutrino energy determination*, CERN-LAA-94-19 (1994).

[16] I.G. Irastorza and J. Redondo, *New experimental approaches in the search for axion-like particles*, *Prog. Part. Nucl. Phys.* **102** (2018) 89 [arXiv:1801.08127].

[17] H.M. Araújo et al., *The MIGDAL experiment: Measuring a rare atomic process to aid the search for dark matter*, *Astropart. Phys.* **151** (2023) 102853 [arXiv:2207.08284].

[18] Particle Data Group, *Review of Particle Physics*, *Prog. Theor. Exp. Phys.* **2022** (2022) 083C01.

[19] FASTER digital modular acquisition system, http://faster.in2p3.fr/.

[20] A.L.M. Silva et al., *X-ray imaging detector based on a position sensitive THCOBRA with resistive line*, 2013 *JINST* **8** P05016.

[21] J.F. Ziegler, M.D. Ziegler and J.P. Biersack, *SRIM – The stopping and range of ions in matter (2010)*, *Nucl. Instrum. Meth. B* **268** (2010) 1818.

[22] F. Sauli, *Gaseous Radiation Detectors: Fundamentals and Applications*, Oxford University Press (2015) [DOI:10.1017/9781009291200].

[23] Photomultiplier tube R8520-406 Hamamatsu Photonics, https://www.hamamatsu.com/us/en/product/optical-sensors/pmt/pmt_tube-alone/metal-package-type/R8520-406.html.

2023 JINST 18 P08005

[24] A. Morozov et al., *A 2D gas scintillation detector for thermal neutrons*, in the proceedings of the *IEEE Nuclear Science Symposium and Medical Imaging Conference*, Anaheim, CA, U.S.A., 27 October–3 November 2012, pp. 1572–1576 [DOI:10.1109/nssmic.2012.6551375].

[25] T. Takahashi et al., *Emission spectra from Ar_3Xe, Ar_3Kr, Ar_3N_2, Ar_3CH_4, Ar_3CO_2 and Xe_3N_2 gas scintillation proportional counters*, *Nucl. Instrum. Meth.* **205** (1983) 591.

[26] RD51 collaboration, *Research on discharges in micropattern and small gap gaseous detectors*, arXiv:0911.0463.

[27] C.A.N. Conde and A.J.P.L. Policarpo, *A gas proportional scintillation counter*, *Nucl. Instrum. Meth.* **53** (1967) 7.

[28] H.A. van Sprang, H.H. Brongersma and F.J. de Heer, *Electron impact induced light emission from CF_4, CF_3H, CF_3Cl, CF_2Cl_2 and $CFCl_3$*, *Chem. Phys.* **35** (1978) 51.

[29] U. Müller, M. Lange, W. Haas and R. Brenn, *Photon/fragment-ion coincidence investigation of the continuous ultraviolet emissions produced by fast ion impact on CF_4 and CHF_3*, *J. Chem. Phys.* **100** (1994) 5550.

[30] L.G. Christophorou, J.K. Olthoff and M.V.V.S. Rao, *Electron Interactions with CF_4*, *J. Phys. Chem. Ref. Data* **25** (1996) 1341.

[31] R.S. Simon., *The Darmstadt-heidelberg Crystal Ball*, *J. Phys. Colloq.* **41** (1980) 281.

[32] S.J.C. do Carmo, F.I.G.M. Borges and C.A.N. Conde, *Performance of Argon-Xenon Mixtures in a Gas Proportional Scintillation Counter for the 0.1–10 keV X-Ray Region*, *IEEE Trans. Nucl. Sci.* **56** (2009) 437.

[33] C.M.B. Monteiro et al., *Secondary Scintillation Yield in Pure Xenon*, 2007 *JINST* **2** P05001 [physics/0702142].

[34] E. Aprile, A.E. Bolotnikov, A.I. Bolozdynya and T. Doke, *Noble Gas Detectors*, John Wiley & Sons (2007).

2023 JINST 18 P08005